A random asymmetric temporal model of multi-agent interactions: Dynamical analysis

Article *in* Physica D Nonlinear Phenomena · July 2003

Impact Factor: 1.64 · DOI: 10.1016/S0167-2789(03)00094-0

3 authors, including:

Christos Emmanouilides
Aristotle University of Thessaloniki
22 PUBLICATIONS **135** CITATIONS
SEE PROFILE

Stathis Kasderidis
Novocaptis Cognitive Systems & Robo…
25 PUBLICATIONS **111** CITATIONS
SEE PROFILE

Available online at www.sciencedirect.com
SCIENCE DIRECT®
Physica D 181 (2003) 102–120
PHYSICA D
www.elsevier.com/locate/physd

A random asymmetric temporal model of multi-agent interactions: dynamical analysis

C.J. Emmanouilides [a,*], S. Kasderidis [b], J.G. Taylor [b]

[a] *Department of Economics, Aristotle University of Thessaloniki, P.O. Box 170, 54006 Thessaloniki, Greece*
[b] *Department of Mathematics, Centre for Neural Networks, King's College, Strand, London WC2R 2LS, UK*

Received 11 February 2002; received in revised form 27 February 2003; accepted 28 February 2003
Communicated by E. Ott

Abstract

We present work in progress on the dynamical analysis of a multi-agent model that allows for temporally distributed asymmetric interactions between agents. The model essentially defines a coupled map lattice in which interactions between local variables obey a random Gaussian law and are transmitted through a gamma pattern of delays. The asymptotic dynamics of the model is investigated employing a dynamic mean field approach. The predictions of the mean field equations are checked numerically through simulations of a finite system of interacting units.

PACS: 05.45.+b; 02.30.Ks

Keywords: Multi-agent interactions; Time delay; Nonlinear dynamics; Coupled map lattices

1. Introduction

In recent years, interest in statistical mechanics models of interactions has grown in many scientific disciplines. Such models include Ising lattices (e.g. [1]), spin-glasses [2], and percolation models [3]. In the social sciences and particularly in economics, several authors have suggested the use of similar model approaches to problems of asset management (e.g. [4]), technological change (e.g. [5]), the diffusion of standards (e.g. [6]), discrete choice theory and econometrics (e.g. [7–9]). In the natural and the life sciences, neural networks is a typical example of statistical mechanical models with widespread use (e.g. [10,11]).

Motivated by the increasing interest in models with interaction, in this paper we study the dynamics of a generic model of behavior in a multi-agent system, where interactions are allowed to be random asymmetric and temporally distributed according to a gamma delay kernel. As such, the model is related to the spin-glass type. We call this model gamma TRRNN (temporal random recurrent neural network). The dynamics of RRNN (random recurrent neural network) models in the absence of time delays have been studied by several authors (e.g. [12–21]). The need to model temporal patterns in the transmission of interactions is suggested in several situations (e.g. Manski [22]

* Corresponding author.
E-mail address: cemman@econ.auth.gr (C.J. Emmanouilides).

0167-2789/03/$ – see front matter
doi:10.1016/S0167-2789(03)00094-0

in an endogenous social interactions setting; Iannacone [23] and Rosser [24, pp. 45–46] in a consumer demand setting; Amit [10] in neural networks and brain research settings).

The first aim of the paper is the investigation of the asymptotic average behavior of a multi-agent system described by a gamma temporal structure. Of particular interest is the bifurcation diagram for the control parameters of the model that describes the system dynamics. Second, we are interested in examining the finite system size properties of the model. While the mean field equations (MFEs) provide information on the bifurcations of the fixed points of the system, and the resulting number of attractors, finite system size simulations can give further insight into the nature of the attractors. They also provide a check of the validity of the mean field theory predictions, and a qualitative assessment of the finite-size effects on system dynamics. These can be of interest in practical situations, where the population is finite, or when it consists of a finite group of homogenous sub-populations interacting under the specified model form (e.g. Geman [25] considers such a case). Third, we wish to examine if the delay structure alters qualitatively the system dynamics with respect to the non-temporal RRNN. The latter case has been studied by Cessac et al. [19], and our line of investigation follows their approach.

The rest of the paper is organized as follows: in Section 2 we formulate the gamma TRRNN model. Section 3 presents the MFEs and the assumptions underlying their derivation. Section 4 discusses the bifurcation structure of the MFEs. Section 5 presents the finite system size simulations and results. Finally, in Section 6 we conclude with a summary of the findings and suggestions for further work.

2. Model formulation

We consider a fully connected system of N agents whose behavior at time period t with respect to a binary action $A \in \{0, 1\}$ is described by a state vector $\{x_i(t)\}_{i=1}^{N}$, $x_i(t) \in [0, 1]$. This continuous formulation of the individual states reflects the presence of a "latent" variable which triggers a binary action when a threshold value is exceeded. In a social-science context, an individual state variable may be viewed as an *attitude* or *opinion*, while in a neural networks context it is the *output* of a neuron. Alternatively, it can be seen as the probability of deciding to perform the action $\{A = 1\}$. The dynamics is in discrete-time, governed by the system of N coupled logistic recurrences

$$x_i(t+1) = S(h_i(t)), \tag{1}$$

where

$$h_i(t) = \sum_{j=1}^{N} \sum_{\tau=0}^{T} J_{ij}(\tau) x_j(t-\tau) - \theta_i(t) \tag{2}$$

is known as *potential*, and

$$S(y) = \frac{1}{2}(1 + \tanh(gy)) = \frac{1}{1+\exp(-2gy)}. \tag{3}$$

A discussion of the derivation of such a logistic model form, and its interpretation in a social-science choice-theoretic context can be found in [8,26]. In model (1), $J_{ij}(\tau)$ is the weight of the state, $x_j(t-\tau)$ of agent j at time $t-\tau$ on the current state, $x_i(t-\tau)$ of agent i. The argument τ, in the weighting coefficients, $J_{ij}(\tau)$, reflects the temporal pattern of the interactions among the agents of the system. $T \in [0, \infty)$ is the maximum delay time, and $\theta_i(t)$ is the external field (or stimulus) on agent i. In Eq. (3), g is a parameter reflecting the degree of randomness in the system, which we call *gain*.

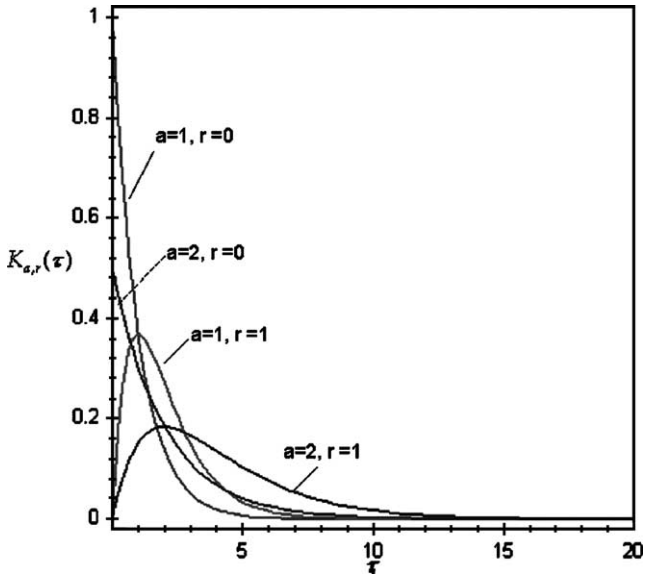

Fig. 1. The gamma delay kernel for scale parameter values $a = 1, 2$ and shape parameter values $r = 0, 1$.

A two-parameter *gamma delay kernel* is assumed, due to its capacity to accommodate a variety of delay patterns (Fig. 1),

$$K_{a,r}(\tau) = \left(\frac{1}{a}\right)^{1+r} \frac{\tau^r \exp(-\tau/a)}{\Gamma(r+1)}, \quad a > 0, \quad r > -1 \tag{4}$$

with mean $a(1+r)$ and variance $a^2(1+r)$, such that

$$J_{ij}(\tau) = K_{a,r}(\tau) J_{ij}, \tag{5}$$

where

$$J_{ij} \backsim N\left(\frac{\bar{J}}{N}, \frac{J^2}{N}\right). \tag{6}$$

That is, we assume that the interaction weights are IID normal random variables, and are distributed over time under a gamma law acting on the fixed (quenched) J_{ij}'s. The matrix $\mathbf{J} = (J_{ij})$ is called the *interaction matrix* of the system (1). The moments of the normal distribution are normalized by the system size to ensure that the sums of the interactions are of order one, O(1), independent of the system size. In such a way, the potentials are bounded and system size independent (i.e. they are intensive variables). Moreover, $\forall i, j = 1, \ldots, N$, $J_{ij} \neq J_{ji}$, $\mathrm{Corr}(J_{ij}, J_{ji}) = 0$, i.e. the interactions are *fully asymmetric* (e.g. [27, Chapter 1]). For simplicity, we assume that the external field is stationary, $\theta_i(t) = \theta_i$, and IID Gaussian

$$\theta_i \backsim N(\bar{\theta}, \sigma_\theta^2). \tag{7}$$

For $r > 0$, the kernel corresponds to the "*strong*" delay case, while for $r = 0$ it corresponds to the "*weak*" delay case (Fig. 1), following the terminology of Cushing [28].

Eqs. (1)–(7) define the *gamma TRRNN model*. This model defines our multi-agent system which is essentially a couple map lattice (e.g. [42]) with time-delayed random couplings; our "agents" correspond to the local variables

of the lattice and the interactions among them to the couplings of the local variables. The control parameter space is $(g, \bar{\theta}, \sigma_\theta, \bar{J}, J, a, r)$. In the following sections we study its dynamic behavior, assuming that $J = 1$, and $\bar{J} = 0$. The assumption $J = 1$ is not restrictive, since a reparameterization $(g \to gJ, \bar{\theta} \to \bar{\theta}/J, \sigma_\theta \to \sigma_\theta/J, \bar{J} \to \bar{J}/J)$ leaves the model equations unchanged. Consequently, the results can be extended to any value of J. The restriction $\bar{J} = 0$ is made in order to facilitate comparison with literature results: the gamma TRRNN is compared with the RRNN model [19]. This value of $\bar{J}$ corresponds to the situation where the probabilities for positive and negative interactions among agents are equal. This is a case in which antagonistic or "snob" behavior ($J_{ij} < 0$), and imitative or "conformist" behavior ($J_{ij} > 0$) are equally likely in the population. Moreover, for $\bar{J} = 0$, due to the distributional specification, it could be the case that for a pair of agents (i, j), $J_{ij} \cdot J_{ji} < 0$.

3. Macroscopic equations

Due to the large number of degrees of freedom and the random nature of the parameters involved, the N-dimensional dynamical system (1), $N \gg 1$, can be viewed as stochastic. In such a system, the main interest is usually in time independent probability measures that describe the asymptotic behavior of the state variables $\{x_i(t)\}_{i=1}^N$ when $N \to \infty, t \to \infty$. Even in the case that the analytical derivation of such measures is feasible, it involves in general assumptions about the correlation structure of the state variables, $x_i(t)$ (e.g. [10,29–31]). In this section we will derive MFEs that describe the dynamic behavior of macroscopic observables of the system's state. For this purpose, we employ a set of independence assumptions which are known in the neural networks literature as "*local chaos hypothesis*" [12,25]. We extend this set of assumptions to account for the particular model form (1). Mean field theory has been shown in many cases to be exact in the asymptotic limit when interactions are long range, or when the system is fully connected [32, Chapter 4].

3.1. Local chaos hypothesis

The "local chaos hypothesis" states (e.g. [25]) that *for large system size, $N \to \infty$, the random variables $\{x_i(t)\}_{i=1}^N$ are nearly independent of each other and of the interaction strengths $\{J_{kl}\}_{k,l=1}^N$*. We will also assume that in the limit, $\forall i = 1, \ldots, N$, (a) the two components of the potentials (2), θ_i and $\sum_{j=1}^N \sum_{\tau=0}^T K_{a,r}(\tau) J_{ij} x_j(t-\tau)$ are independent, and (b) the cross-correlations between the state variables are negligible, i.e. $\lim_{N\to\infty} E_N[x_i(t), x_j(t-\tau)] = 0$. Then, under the IID Gaussian assumptions (6) and (7), the potentials are approximately IID Gaussian random variables at each time period t. However, the distribution of the state variables, $x_i(t+1) = S(h_i(t))$, does not appear to have any closed form.

We have checked numerically the validity of the above assumptions, for a variety of control parameter values. The results, given in Appendix A, support the validity of the assumptions.

3.2. Mean field equations

The assumptions we made allow the derivation of equations for the moments of the $x_i(t)$'s distribution. Details are given in Appendix B. The equation for the nth order moment of the distribution of $\{x_i(t)\}_{i=1}^N$ becomes

$$m^{(n)}(t+1) = \int_{-\infty}^{+\infty} G\left[S\left(u\sqrt{\sum_{\tau=0}^{T} K_{a,r}(\tau) J^2 m^{(2)}(t-\tau) + \sigma_\theta^2} + \sum_{\tau=0}^{T} K_{a,r}(\tau)\bar{J} m^{(1)}(t-\tau) - \bar{\theta}\right)\right]^n \mathrm{d}u, \quad (8)$$

where $G = (1/\sqrt{2\pi})\exp(-u^2/2)$ is the Gaussian measure, and $S(\cdot)$ is given by (3). It can be seen that the mean field dynamics is determined by the first two moments of the distribution. In the present study we restrict our interest to

the behavior of the first moment, $m^{(1)}(t)$, the average state of the system. Its dynamics is closely linked with those of the second moment through their coupling, and it turns out that they exhibit similar features (e.g. bifurcation structure). Thus, in our analysis, we employ the equations for the first two moments only, which we term MFE. Eq. (8) are similar in form to the dynamic MFEs of Crisanti and Sompolinski [17], and to those of Cessac et al. [19]. They are valid for any point in the parameter space $(g, \bar{\theta}, \sigma_\theta, \bar{J}, J, a, r)$.

Eq. (8) describes a stochastic process. This process is the evolution path of an ensemble of N-dimensional systems (1). The averaging in these moment equations is over the ensemble (i.e. draws of interaction matrices, and external fields). Due to this fact, the MFE are expected to exhibit simpler dynamics than individual N-dimensional systems. As our numerical simulations show (see Section 4), the MFE dynamics is predominantly regular; i.e. possesses only fixed points. More complex MFE dynamics (e.g. periodic, quasiperiodic, or strange attractors), if present, could correspond to the case that the support of the distribution of the x_i's would not be an invariant set; as such it would be a union of disconnected non-invariant sets, with possible fractal structure (e.g. [33,34]). Fixed points for the first two moment equations, may correspond to more complex attractors for the system (1). Such attractors could be detected only through numerical simulations of the N-dimensional system.

4. Bifurcations of the MFEs

In this section we study the asymptotic solutions of the MFE (8). In particular, we provide two classes of bifurcation diagrams which summarize the asymptotic dynamics of the ensemble in the control parameter space. The first class depicts the variation of the first moment, $m^{(1)}(\infty)$, against one of the control variables, all other things being held constant. The second class shows the type of bifurcation occurring in $m^{(1)}(\infty)$ against two control variables. It is parameterized by a third control variable. The diagrams of the first class correspond to distinct regions of the second class' diagrams. Finally, we examine the effects of the parameter σ_θ and the delays on the bifurcation structure.

We simulate the MFE by drawing several initial conditions, for $m^{(1)}$, $m^{(2)}$, and iterating (8) for a number of time steps (typically 2000) in order to reach an asymptotic state. The sampling of the parameter space is performed in the following manner: $a \in \{1, 2, 3, 4\}$, $r \in \{0, 1\}$, $g \in [0, 15]$, $\bar{\theta} \in [0, 1]$, and $\sigma_\theta \in [0, 1]$. The parameter g varies with step size 0.25, $\bar{\theta}$ and σ_θ with step sizes 0.025, respectively. Close to bifurcation points we sample the parameter space more densely by decreasing the step sizes.

The dynamics converges to fixed point attractors. In a few cases we observed periodic points, or even irregular motions of small amplitude (typically of $O(10^{-3})$) near critical points, and for larger values of σ_θ. We have not yet established their significance, and further investigation is required to rule out that they are numerical artifacts. If they are genuine features, we conjecture that their presence is due to the time delays.

We find that the bifurcation behavior of the MFE is qualitatively similar to that of the RRNN case: the observed bifurcations are of saddle-node type and their appearance divides the $(\bar{\theta}, g)$ plane into four regions where the MFE exhibits distinct dynamics (Figs. 2 and 3). The two critical lines (α), (δ), indicate the minimum g value required (for fixed $\bar{\theta}$) for the onset of a saddle-node bifurcation. In region I, there is only one stable fixed point solution. A typical bifurcation diagram of the $m^{(1)}(\infty)$ corresponding to $(\bar{\theta}, g)$ parameters in this region is given in Fig. 4a. In region II there are two stable fixed points. A diagram for $m^{(1)}(\infty)$ in this parameter region is given in Fig. 4b. As parameter $\bar{\theta}$ increases (for appropriate values of g), line (α) is crossed, and a saddle-node bifurcation generates a second stable fixed point located beneath the initial one. In region III, bounded by the two vertical lines (β), (γ) in the case of the RRNN model, there are again two stable fixed points, generated by the sequence of one saddle-node bifurcation, and its inverse. The second bifurcation occurs when line (δ) is crossed within region III. These two bifurcations collapse at the cusp point (note that due to the finite step size this sequence is not fully depicted). A bifurcation diagram for this case is shown in Fig. 4c. As $\bar{\theta}$ increases further, we enter again into region II, where

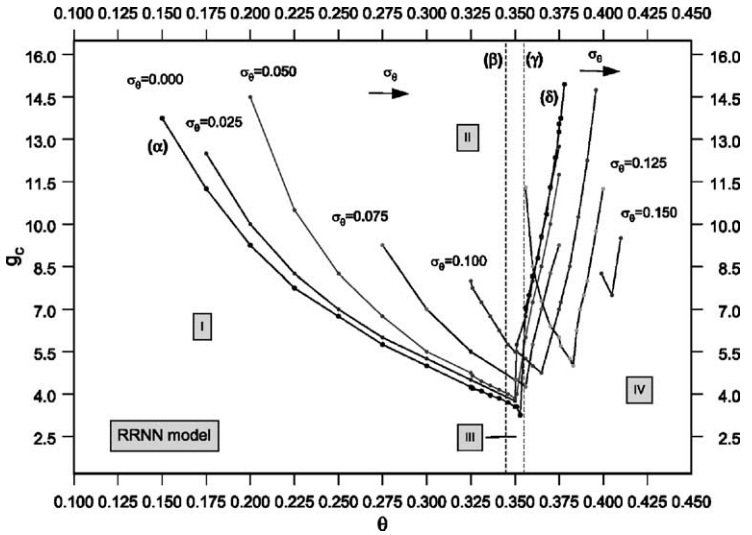

Fig. 2. Critical lines for the onset of saddle-node bifurcations and the corresponding regions of the MFE dynamics in the $(\bar{\theta}, g)$ parameter space, parameterized by σ_θ, for the RRNN model. The effect of σ_θ is similar for the gamma TRRNN model.

two fixed points coexist, but the corresponding diagrams (Fig. 4d) are now reversed (with respect to those before the entry into region III). Finally, when line (δ) is crossed, we enter the monostable region IV, where only the lower fixed point of Fig. 4d survives (Fig. 4e).

4.1. *Effect of the external field heterogeneity, σ_θ*

Our analysis provides insights about the effects of the heterogeneity parameter σ_θ on the bifurcation structure of the MFE. These effects are qualitatively the same for both the gamma TRRNN and the RRNN models. They are depicted in Fig. 2, which was derived for the latter model. The results are as follows:

(a) Increasing σ_θ shrinks the bistability region II and shifts it to the right, towards higher values of $\bar{\theta}$.
(b) The range on the $\bar{\theta}$-axis for which the two critical lines practically coexist (region III) also shrinks, and the critical lines become steeper.
(c) For large σ_θ, region III collapses to a point, the cusp point. There, hysteresis loops have been observed for the gamma TRRNN model (see Fig. 4f).
(d) The critical lines (α) and (δ) are shifted towards larger values of g with increasing σ_θ.
(e) For constant σ_θ, the value of g (against $\bar{\theta}$) for the transition from region I→II decreases, while for the transition II→IV increases, respectively.

In Fig. 2, the arrows indicate the direction of the shift of the critical lines when σ_θ increases.

4.2. *Effect of the delays*

The presence of the kernel results to a shift of the critical lines (α) and (δ), as shown in Fig. 3. For the "weak" delay case ($r = 0$), the shift is towards the right side of the $\bar{\theta}$-axis, while for the "strong" case ($r = 1$) it is towards the left side. The results are as follows:

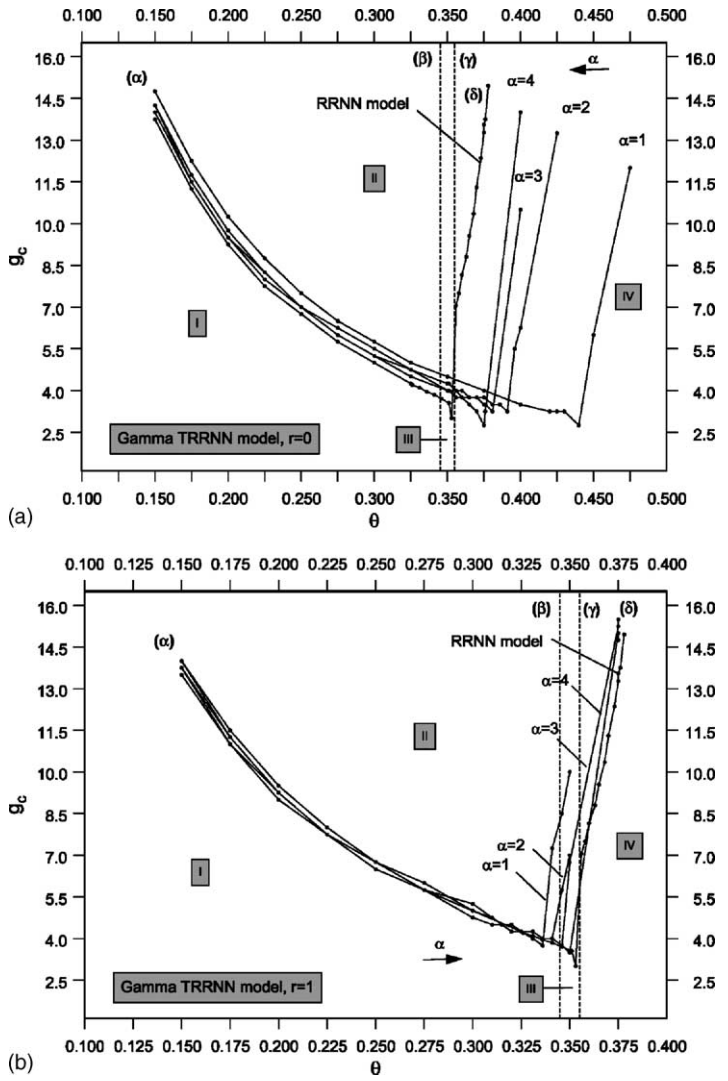

Fig. 3. Critical lines for the onset of saddle-node bifurcations and the corresponding regions of the MFE dynamics in the $(\bar{\theta}, g)$ parameter space, parameterized by α, for the gamma TRRNN model. (a) The "weak" delay case, $r = 0$, and (b) the "strong" delay case, $r = 1$. In both diagrams $\sigma_\theta = 0$.

(a) "Weak" delays:
   (a) The bistability region (II) shrinks upwards and towards the left side of the $\bar{\theta}$-axis when the delay strength a increases. This is due to a shift of the critical line (δ) to the left.
   (b) The width of region III shrinks as a increases.
   (c) The cusp point occurs at slightly higher values of g as a increases.

(b) "Strong" delays:
   (a) The bistability region (II) widens and shifts upwards and towards the right side of the $\bar{\theta}$-axis, when the delay strength a increases.
   (b) The width of region III increases marginally as a increases.

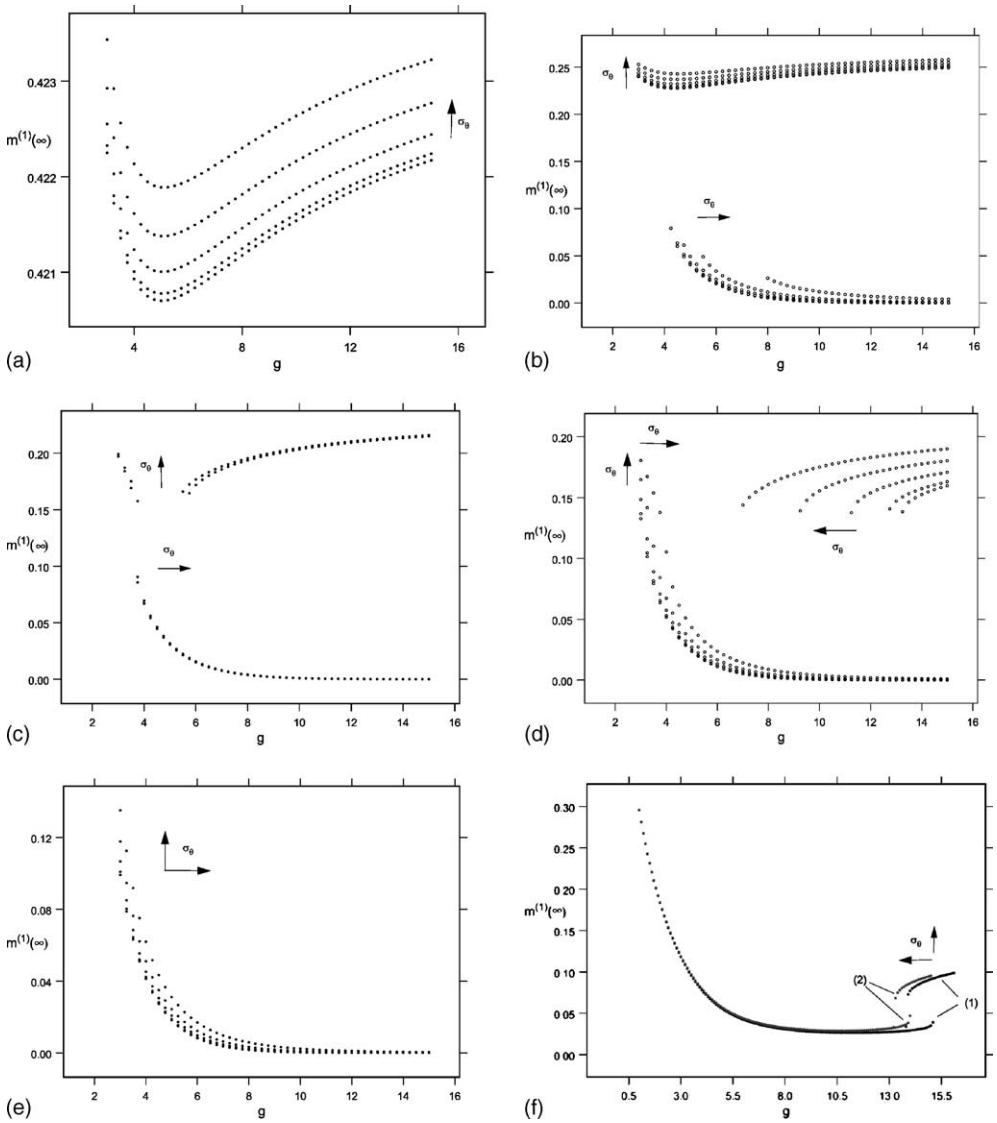

Fig. 4. Typical bifurcation diagrams of the observable, $m^{(1)}(\infty)$, against g for the gamma TRRNN model. The arrows indicate the direction of shift of the bifurcation diagrams when σ_θ increases.

(c) The cusp point moves slightly downwards as a increases.

The arrows in Fig. 3 indicate the direction of the shift of the critical line (δ) when a increases.

5. Finite system size simulations

The aim of this section is to explore the finite system size dynamics, their agreement with the MFE predictions, and the possible effects of the delays. In particular, we want to compare the gamma TRRNN and RRNN models. To achieve this aim, we iterate the N-dimensional system (1), for $N = 50$, for selected points of the parameter space.

Then, we perform a dynamical systems' analysis of the results. Additional simulations are performed for system sizes $N = 75$, and 100. Due to computational burden these results are less extensive.

The simulation strategy is the following: we examine four pairs of kernel parameters, for $a = 1, 2$ and $r = 0, 1$. For each pair, we sample the parameter space $(g, \bar{\theta})$ by letting g to vary over the interval $[1, 15]$ with step size 0.5, $\bar{\theta}$ to vary over $[0, 0.5]$ with step 0.05. We let $\sigma_\theta = 0$. At each point of the parameter space we draw at random M realizations ($M = 100$). A realization consists of an interaction matrix, a vector of external fields, and initial conditions for the individual state variables $\{x_i(t_0)\}_{i=1}^N$. Each realization is indexed by $k = 1, \ldots, M$. We iterate the N-dimensional system (1) for a sufficient number of time steps, until convergence is reached. The number of steps is set to $T_s = 5000$. At each time step, $t = 1, \ldots, T_s$, we calculate the average activity of the system, $m_N^{(k)}(t) = (1/N) \sum_{i=1}^N x_i^{(k)}(t)$, which is the observable of interest, and corresponds to the first order moment of the MFE (8). We term the vector $\{m_N^{(k)}(t)\}_{t=1}^{T_s}$ an orbit. In the subsequent analysis we keep the part of the orbit after the transient.

5.1. Steady states—attractors

To classify the attractors of the system, we use the *Takens' phase space reconstruction method* [35] for the observed time series, $m_N(t)$. This time series is embedded in an appropriate phase space. The dimensionality of this space is found by using the method of *false neighbors* (for details, see [36]). In such a way we determine the number and type of (possibly co-existing) attractors at each point of the control parameter space. There are three classes of attractors: fixed points, periodic points, and irregular (including quasiperiodic attractors, strange attractors, and high dimensional chaotic attractors—see Section 5.1.2).

5.1.1. Distribution of attractors

In this section we study the distributions of the observed attractors for different values of the control parameters. Such distributions describe the most probable dynamics, and provide insights about the bifurcation structure of the system due to the change of the parameters. In particular, when more than one co-existing attractors are present, the probability of their occurrence is directly related to the size of their basins.

As intuition suggests, the dynamics of the average state, $m_N^{(1)}(t)$, of a finite system is consistent with the dynamics of the individual states, $\{x_i(t)\}_{i=1}^N$; fixed points dynamics for $m_N^{(1)}(t)$ is the outcome of fixed point dynamics of the individual states. Periodic motions result as a mixture of fixed points and periodic dynamics of the individual states. Irregular dynamics is the average of the predominantly irregular individual state dynamics, that generally co-exist with few individual fixed points and periodic motions. Fig. 5 illustrates these intuitive results for three typical examples of irregular dynamics.

First, we compare the simplest gamma TRRNN model (for $a = 1, r = 0$) with the RRNN. Then, we compare the three different gamma TRRNN models corresponding to the respective pairs of kernel parameters, with the simplest one, i.e. we examine the effects of the delay structure.

(a) Comparison between the RRNN and the gamma TRRNN model with $a = 1, r = 0$: In Fig. 6 the distributions of the three categories are given for the two models. The results are as follows:
   (a) *Fixed points*: Fixed points are the only type of dynamics observed for both models when $g < 3$. The frequency of appearance of fixed point attractors is higher in the gamma TRRNN model than in the RRNN, for $\bar{\theta} < 0.4$, and for any value of the gain parameter, g. In the first model, when $\bar{\theta} < 0.4$, fixed points persist for all values of g, while in the second they disappear. For $\bar{\theta} \geq 0.4$ almost all the attractors are fixed points, for both models, independent of g. The frequency declines with increasing g for both models, but the decline is faster for the RRNN model.

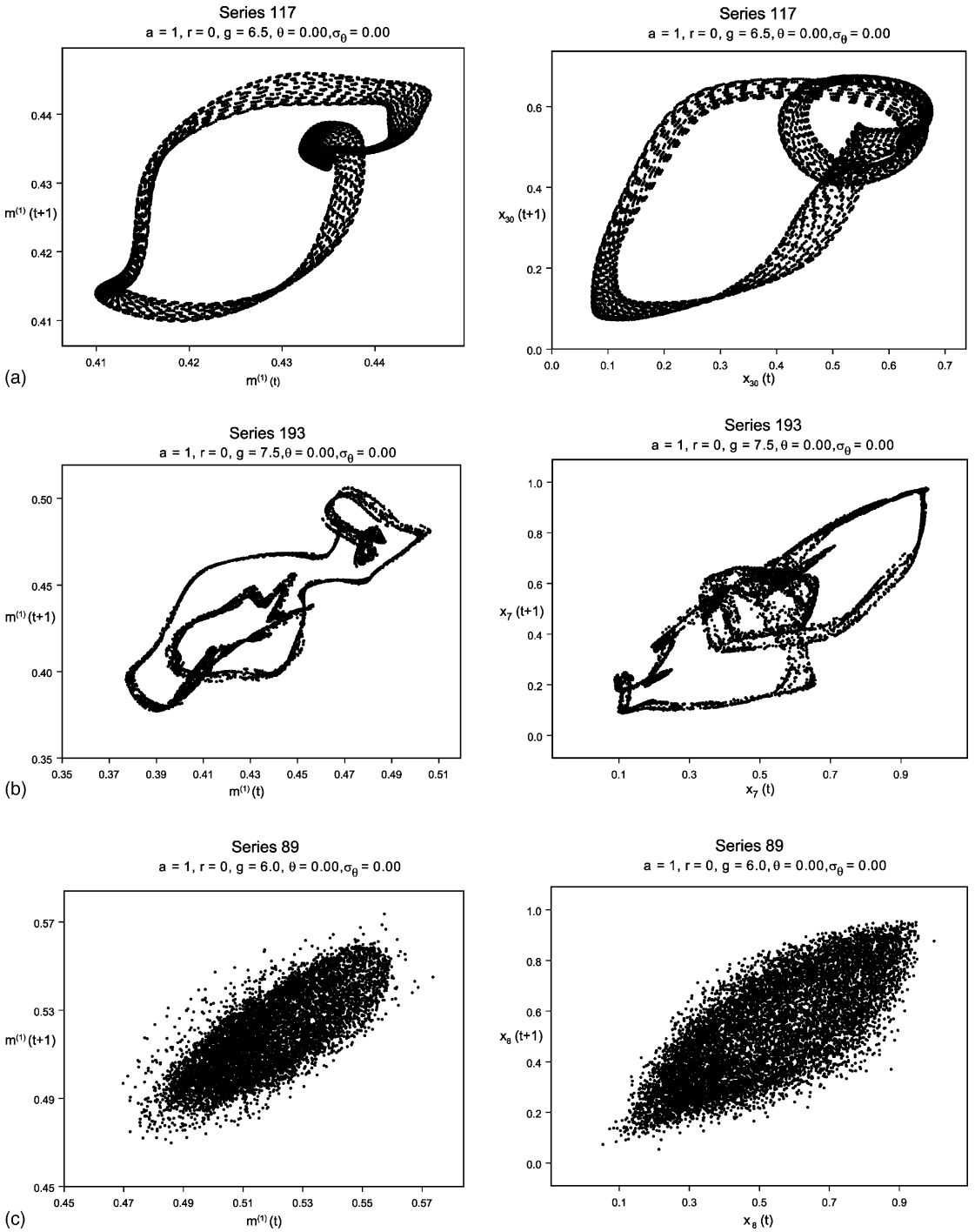

Fig. 5. Examples of irregular dynamics for three finite systems of size $N = 50$. The left panels correspond to the dynamics of $m_N^{(1)}(t)$, and the right ones to the dynamics of representative individual states $x_i(t)$, $i \in \{1, \ldots, N\}$ in each system. As expected, the individual state dynamics is consistent with the dynamics of the average state.

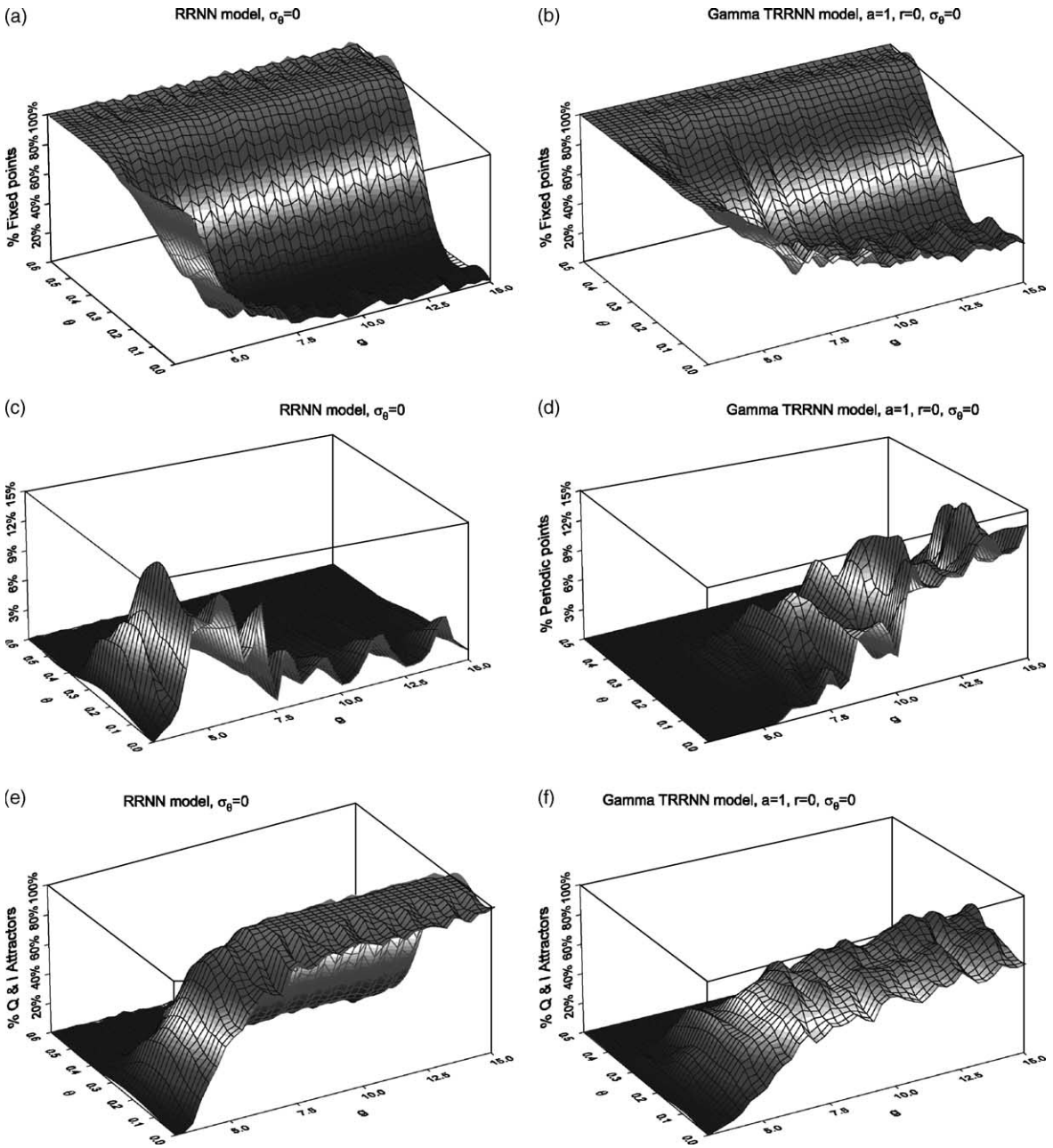

Fig. 6. Attractors of the RRNN and the gamma TRRNN models (left and right panels, respectively) in the $(g, \bar{\theta})$ parameter space for $N = 50$, $\sigma_\theta = 0$.

(b) *Periodic motions*: The frequency of appearance of periodic points in the gamma TRRNN model is near zero for all $\bar{\theta}$ when $g \leq 6$, while for larger g it is generally increasing. When $\bar{\theta} \geq 0.4$ periodic orbits disappear, while for $\bar{\theta} < 0.4$ the frequency is higher for smaller values of $\bar{\theta}$, for almost all values of the gain parameter. For the RRNN model, the situation is different: for $\bar{\theta} > 0.3$ periodic orbits disappear, but for $\bar{\theta} \leq 0.3$ most

periodic orbits occur for $g < 7.5$, while their frequency decreases for $g \geq 7.5$ and becomes practically zero.

(c) *Irregular motions*: These motions are more frequently encountered in the RRNN model. For this model, when $\bar{\theta} \leq 0.2$, their frequency increases with g, at a rate that is almost independent of $\bar{\theta}$. It then reaches a plateau for some value of g that is smaller for larger values of $\bar{\theta}$. For $\bar{\theta} \in [0.3, 0.4)$, their frequency declines rapidly, and when $\bar{\theta} > 0.4$ they disappear. For the gamma TRRNN the pattern is similar.

(b) Effects of the delays: For simplicity of presentation we do not provide the detailed results of this analysis. We give only the qualitative findings for each pair of kernel parameters for each class of dynamics, as compared to those of the simplest case $a = 1, r = 0$.

(a) *"Strong" delay with parameters* $a = 1, r = 1$: The frequency of fixed points has the same qualitative characteristics (i.e. pattern of change with the parameters $(\bar{\theta}, g)$) with those of the simplest case. Their values are similar for any value of $\bar{\theta}$ and g. Periodic orbits are less frequent (less than 6% for any $\bar{\theta}$ and g). The frequency of the irregular motions is slightly higher on average. It appears that the periodic orbits destabilize and become irregular through more frequent Hopf bifurcations.

(b) *"Weak" delay with parameters* $a = 2, r = 0$: The fixed points appear more frequently than in the simplest case. Periodic orbits are less frequent (less than 3% for any $\bar{\theta}$ and g). Irregular attractors are also less frequent. In this case the dynamics is more regular.

(c) *"Strong" delay with parameters* $a = 2, r = 1$: In this case, the periodic orbits completely disappear. The frequency of irregular attractors is generally increasing with g for constant $\bar{\theta}$, while at the value $\bar{\theta} = 0.2$ it initially increases up to $g = 9$, and then decreases. This strange behavior has not been observed for other kernel parameter values, and deserves further investigation, since it may indicate some structural change in the system's properties. The dynamics is more regular than any other pair of kernel parameters.

A general conclusion that can be drawn, is that the presence of delays results to a predominace of fixed point dynamics, and that the periodic orbits practically disappear. The latter fact indicates a lower probability of flip bifurcations in the gamma TRRNN model.

5.1.2. Route to chaos

Observed irregular motions are of three types: quasiperiodic, low dimensional chaotic (strange attractors), and higher dimensional chaotic. Low dimensional chaotic orbits have fractal structure and are embedded in phase spaces with dimensionality from 3 to 5. Higher dimensional chaos behaves more like an IID stochastic process, and typically exists in dimensions larger than or equal to 7. These attractors have passed the BDS test [37], and other criteria for the IID property. The dimensionality of both types of chaotic motions increases slightly with increasing system size.

Examining the destabilization of fixed points through a sequence of bifurcations, we are able to determine the route to chaos. We found this route to be predominantly the quasiperiodic one [38]. Cascades of Hopf bifurcations appear, as the value of g increases, in agreement with Cessac et al. [19], for the RRNN model. For smaller system sizes, the onset of the quasiperiodic route can be through an initial pitchfork or flip bifurcations instead of a Hopf.

Additional to the study of the bifurcation sequence we studied the increase in complexity of the chaotic attractors. We calculated the Lyapunov exponents employing two well-known methods [39,40]. The Lyapunov exponents consistently increase with increasing g (Fig. 7). We present results for $\bar{\theta} = 0$, $\sigma_\theta = 0$, and for all four pairs of kernel parameters. More detailed results for other values of $\bar{\theta}$ and σ_θ will be presented elsewhere. In the finite system size simulations, we observed several chaotic orbits for each value $g > 5$ used. This is due to the fact that the number of initial conditions we used ($M = 100$) is greater than the possible number of observable attractors. Every data point in Fig. 7 depicts the calculated maximal Lyapunov exponent corresponding to each one of these chaotic orbits. The line is a local regression fit (e.g. [41]) to the data points.

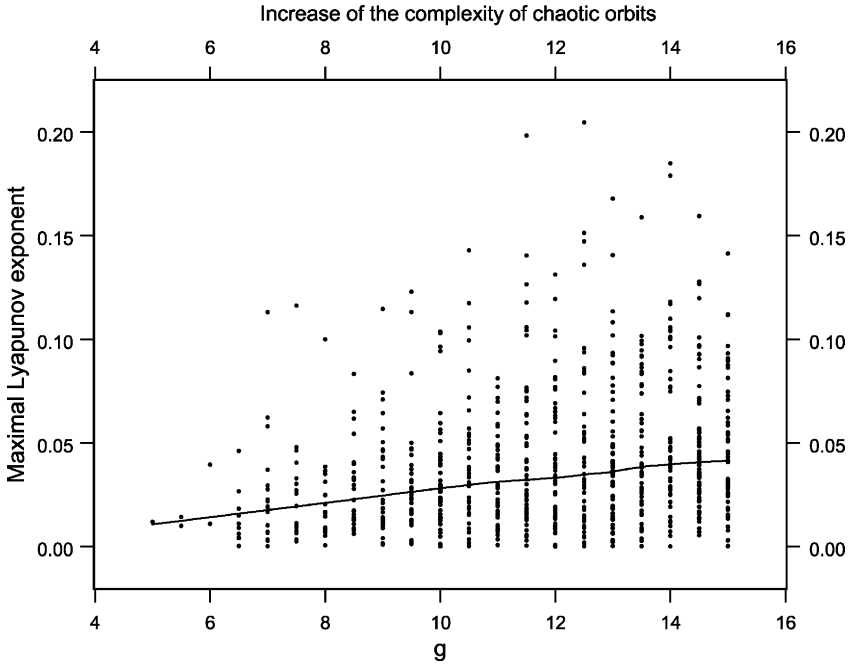

Fig. 7. Estimated maximal Lyapunov exponents for the chaotic attractors of the gamma TRRNN model (all four pairs of kernel parameters), for $\bar{\theta} = 0$, and $\sigma_\theta = 0$.

5.2. *Agreement with the MFE*

The number of attractors of the system (1) for large system size, and a given point of the control parameter space is predicted by the MFE to be either one or two (see Section 4). We checked whether this is the case for finite-size systems, by drawing an ensemble of 30 fixed networks (i.e. draws of interaction matrices and external fields). Then, we iterated them until convergence, for a set of initial conditions for the individual state variables at each sampled point of the control parameter space.

We found that for $N = 50$, the observed number of attractors in the four regions of the MFE bifurcation diagrams (Figs. 2 and 3) is in agreement with the MFE predictions. However, sometimes two attractors are found in locations of these diagrams where one attractor is expected, e.g. a fixed point (or a periodic point) co-existing with a more complex attractor (quasiperiodic or strange attractor). When we increase the system size to $N = 100$, such effects disappear, and the agreement with the MFE predictions is full. Thus, we may attribute these effects to the finite system size.

The magnitude of the observable $m^{(1)}(\infty)$, and the values of g where the two types of saddle-node bifurcations occur (lines (α), (δ) in Figs. 2 and 3), are also generally in good agreement with the MFE predictions.

6. Concluding comments

We examined the asymptotic average dynamics of the gamma TRRNN model, and derived bifurcation diagrams for the control parameters. We found that the effect of the heteregoneity parameter, σ_θ, is a shrinkage of the region in the $(\bar{\theta}, g)$ plane in which bistability appears. The effects of the delays on the structure of the bifurcation diagrams

was also assessed. We did not find any qualitative difference in the asymptotic dynamics between the RRNN and gamma TRRNN models. The finite system size simulations showed that in general there is agreement between the MFE predictions about the number of co-existing attractors, the magnitude of the observable $m^{(1)}(\infty)$, and the critical values of the parameters for the onset of bifurcations.

For a range of the control parameters, we classified the attractors of the finite system, and we examined the route to chaos, which is the quasiperiodic one, as in the RRNN case. Lyapunov exponents were calculated for the chaotic attractors of the gamma TRRNN models. The finite system size dynamics of the gamma TRRNN model were found to be more regular than those of the simpler RRNN model. It was observed that periodic orbits are destroyed when the delay depth increases (for $a \geq 2$ and $r = 1$), indicating that the onset of the quasiperiodic route to chaos is through Hopf bifurcations only, even for small system sizes. A peculiar feature was observed for $a \geq 2, r = 1$; the increase in the complexity of motions shows a non-monotonous variation with the gain parameter, g, near a value of the average external field, $\bar{\theta}$. This feature that is not present in the RRNN model, deserves further investigation. Further research is needed in order to examine the system dynamics in other regions of the control parameter space, and thus to derive a more complete picture of the model's properties. Of particular interest is the study of the case $\bar{J} > 0$, which is relevant in several social-science situations.

Appendix A. Numerical test of the "local chaos hypothesis"

This appendix illustrates the numerical checking of the "local chaos hypothesis" of Section 3. The validity of the assumptions was checked through the corresponding correlation coefficients. More specifically, we draw many sets of interaction strengths $\{J_{ij}\}_{i,j=1}^{N}$ and initial conditions for the state variables, $\{x_i(0)\}_{i=1}^{N}$ for varying system sizes $N \in [5, 150]$,[1] and several points in the control parameter space $(g, \bar{\theta}, \sigma_\theta, \bar{J}, \alpha, r)$. Then, for each such draw, we iterate the system of Eq. (1) for sufficiently long time steps. The details of the subsequent steps follow.

(a) *Assumption* $\lim_{N\to\infty} C_N[J_{ij}, x_j(t-\tau)] = 0$. For a system of size N and a particular point in the control parameter space, the calculation of the correlations between state variables and interaction strengths is done in the following manner. At a time step t_d, which may correspond to an equilibrium or a transient state of the dynamics, we pick the values of a single state variable $x_i(t_d)$ and one of the interaction strengths J_{ij}. The aim is to form a large sample (with size M) of pairs of state variables $\{x_i^{(r)}(t_d)\}_{r=1}^{M}$, and interaction strengths $\{J_{ij}^{(r)}\}_{r=1}^{M}$. If these two variables are uncorrelated, then the property holds for all pairs of interaction strengths and state variables. For a point in the control parameter space, the dynamics, depending on the draw of initial conditions and interaction strengths, can be simple (e.g. fixed points) or more complex (e.g. strange attractors). Whenever draws lead to more complex attractors, we select these draws to form our sample of state variables and interaction strengths. Then, we calculate the absolute correlation coefficients

$$|\hat{C}_N^{(M)}(J_{ij}, x_i(t_d))| = \frac{\left|\sum_{r=1}^{M}(x_i^{(r)}(t_d) - \overline{x_i^{(r)}(t_d)})(J_{ij}^{(r)} - \overline{J_{ij}^{(r)}})\right|}{\sqrt{\sum_{r=1}^{M}(x_i^{(r)}(t_d) - \overline{x_i^{(r)}(t_d)})^2 \sum_{r=1}^{M}(J_{ij}^{(r)} - \overline{J_{ij}^{(r)}})^2}}. \tag{A.1}$$

In our study we used $t_d = 500$, $M = 500$. The numerical results provide support of the assumption $\lim_{N\to\infty} C_N[J_{ij}, x_j(t-\tau)] = 0$. Indeed, in Fig. 8 we see that the correlations decline with system size. This pattern was observed in all the points of the control parameter space where we performed numerical calculations.

[1] Simulations for system sizes above $N > 150$ become exponentially demanding in computational resources.

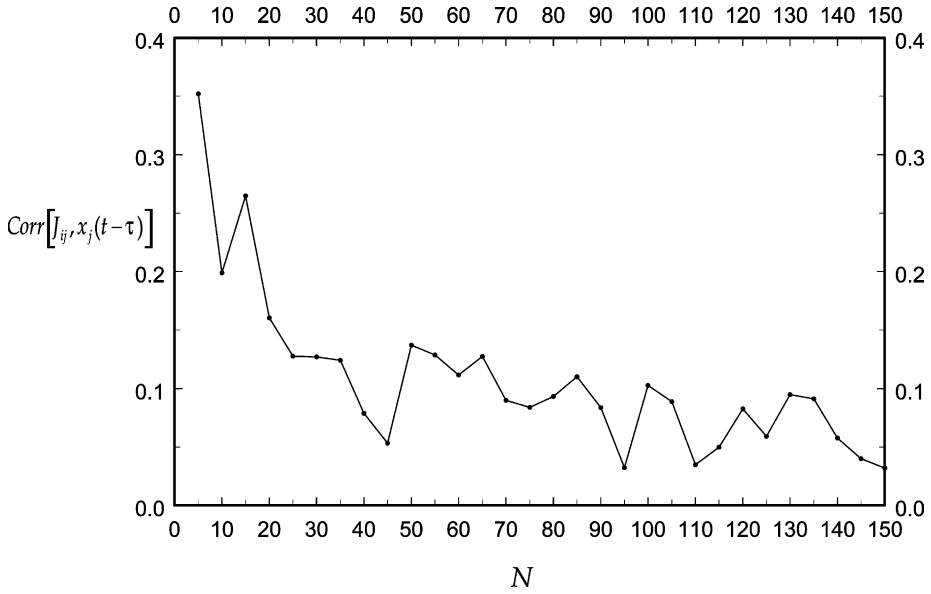

Fig. 8. Correlations between interaction strengths, J_{ij}, and state variables, $x_j(t-\tau)$ against system size, N, for $a = 1, r = 0, \bar{\theta} = 0, \sigma_\theta = 0$. Averaging over $M = 500$ systems.

(b) *Assumption* $\lim_{N\to\infty} C_N[x_i(t-\tau), x_j(t-\tau')] = 0$. For a system of size N and a particular point in the control parameter space, we calculate the cross-correlations between the state variables as follows. We select a block of units i, j with size $d \leq N$, $i, j = 1, \ldots, d$. Then for each selected draw, $r = 1, \ldots, M$, we take a window of size n of the system's iterated dynamics. In this window, and for a number of lags l that are determined by the delay kernel shape, $l = 0, \ldots, \max\{\tau : K_{a,r}(\tau) > 0\}$, we pick the lagged state variable values $x_i^{(r,N)}(t-l)$. In such a way we sample M times d time series of length n. Then we calculate the absolute average block cross-correlations

$$|\hat{R}_{ij}^{(d,N,M)}(l)| = \frac{1}{M}\sum_{r=1}^{M} |\hat{R}_{ij}^{(r,N)}(l)|, \tag{A.2}$$

where

$$\hat{R}_{ij}^{(r,N)}(l) = \frac{\hat{C}_{ij}^{(r,N)}(l)}{\sqrt{\hat{C}_{ii}^{(r,N)}(0)\hat{C}_{jj}^{(r,N)}(0)}}, \tag{A.3}$$

with cross-covariances

$$\hat{C}_{ij}^{(r,N)}(l) = \frac{1}{n}\sum_{t=l+1}^{n} (x_i^{(r,N)}(t-l) - \bar{x}_i^{(r,N)})(x_j^{(r,N)}(t-l) - \bar{x}_j^{(r,N)}). \tag{A.4}$$

Our calculations where done with values $d = 5$, $M = 500$, and $n = 500$. Again, the numerical results provide support for the assumption $\lim_{N\to\infty} C_N[x_i(t-\tau), x_j(t-\tau')] = 0$. In Fig. 9 we see that the zero lag block cross-correlations decline with system size, and in Fig. 10 we see a similar pattern for the non-zero lag case. Similar patterns were observed in other points of the control parameter space.

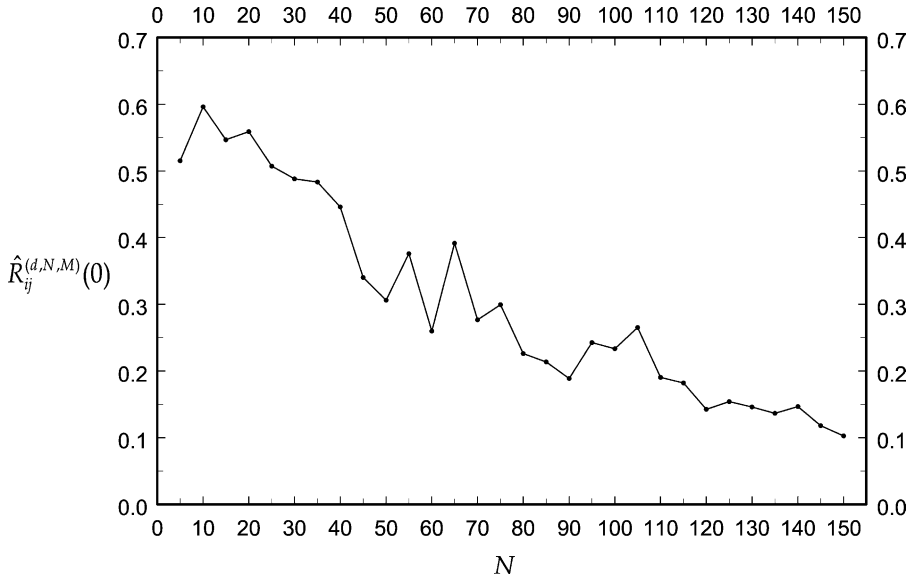

Fig. 9. Zero lag ($\tau = 0$) block cross-correlations against system size, N, for $a = 1$, $r = 0$, $\bar{\theta} = 0$, $\sigma_\theta = 0$. Averaging is over $M = 500$ systems and block size $d = 5$.

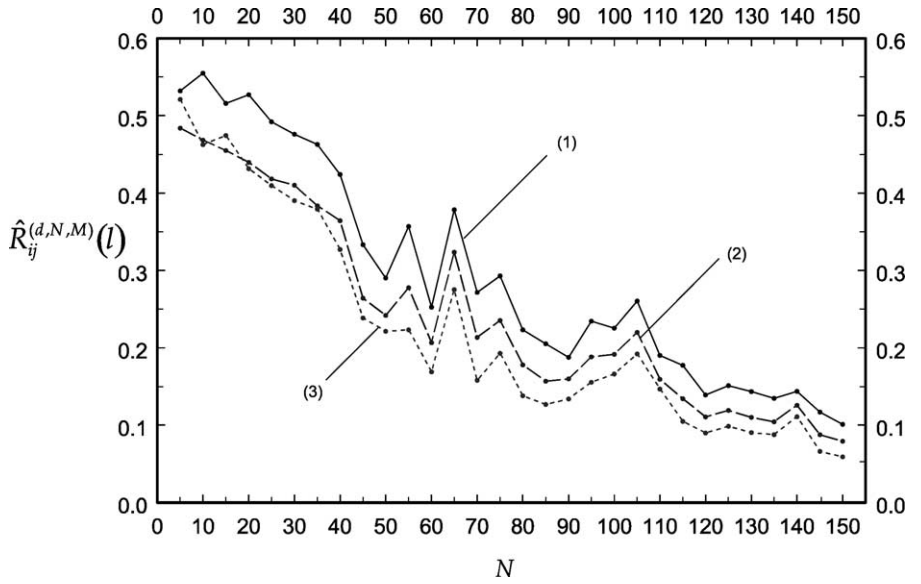

Fig. 10. Block cross-correlations against system size, N, for $a = 1$, $r = 0$, $\bar{\theta} = 0$, $\sigma_\theta = 0$. Averaging is over $M = 500$ systems and block size $d = 5$. Line (1) corresponds to lag $\tau = 1$, (2) to $\tau = 5$, and (3) to $\tau = 11$.

Appendix B. Mean field equations

In this appendix we sketch the analytical derivation of the mean field equations (8). Under the assumptions of Section 3, the random variables $h_i(t)$ are IID normal,

$$h_i(t) \backsim N(\mu_N(t), v_N(t)). \tag{B.1}$$

Denote the first two moments of the distribution of $\{x_i(t-\tau)\}_{i=1}^N$ as $m_N^{(1)}(t-\tau) = E_N[x_i(t-\tau)]$, and $m_N^{(2)}(t-\tau) = E_N[x_j^2(t-\tau)]$. Then, the following relations hold for the mean and variance of the potentials $h_i(t)$:

$$\begin{aligned}\mu_N(t+1) &= E_N[h_i(t+1)] = \sum_{j=1}^{N}\sum_{\tau=0}^{T} K_{a,r}(\tau)E_N[J_{ij}]E_N[x_j(t-\tau)] - E_N[\theta_i] \\ &= NE_N[J_{ij}]\sum_{\tau=0}^{T} K_{a,r}(\tau)E_N[x_j(t-\tau)] - E_N[\theta_i] = \bar{J}\sum_{\tau=0}^{T} K_{a,r}(\tau)m_N^{(1)}(t-\tau) - \bar{\theta},\end{aligned} \tag{B.2}$$

and

$$\begin{aligned}v_N(t+1) &= \mathrm{var}_N[h_i(t+1)] = \mathrm{var}\left[\sum_{j=1}^{N}\sum_{\tau=0}^{T} K_{a,r}(\tau)J_{ij}x_j(t-\tau) - \theta_i\right] \\ &= \mathrm{var}\left[\sum_{j=1}^{N}\sum_{\tau=0}^{T} K_{a,r}(\tau)J_{ij}x_j(t-\tau)\right] + \mathrm{var}[\theta_i] + 2\mathrm{cov}\left[\sum_{j=1}^{N}\sum_{\tau=0}^{T} K_{a,r}(\tau)J_{ij}x_j(t-\tau), \theta_i\right].\end{aligned} \tag{B.3}$$

Employing the assumptions of Section 3, with some algebra we get

$$\begin{aligned}&\mathrm{cov}\left[\sum_{j=1}^{N}\sum_{\tau=0}^{T} K_{a,r}(\tau)J_{ij}x_j(t-\tau), \theta_i\right] \\ &= E_N\left[\theta_i\sum_{j=1}^{N}\sum_{\tau=0}^{T} K_{a,r}(\tau)J_{ij}x_j(t-\tau)\right] - E_N\left[\sum_{j=1}^{N}\sum_{\tau=0}^{T} K_{a,r}(\tau)J_{ij}x_j(t-\tau)\right]E_N[\theta_i] \\ &= \sum_{j=1}^{N}\sum_{\tau=0}^{T} K_{a,r}(\tau)E_N[J_{ij}]E_N[x_j(t-\tau)]E_N[\theta_i] - \sum_{j=1}^{N}\sum_{\tau=0}^{T} K_{a,r}(\tau)E_N[J_{ij}]E_N[x_j(t-\tau)]E_N[\theta_i] = 0.\end{aligned} \tag{B.4}$$

Hence,

$$\begin{aligned}v_N(t+1) &= \mathrm{var}\left[\sum_{j=1}^{N}\sum_{\tau=0}^{T} K_{a,r}(\tau)J_{ij}x_j(t-\tau)\right] + \mathrm{var}[\theta_i] = \sum_{j=1}^{N}\sum_{\tau=0}^{T} K_{a,r}(\tau)\,\mathrm{var}[J_{ij}x_j(t-\tau)] + \sigma_\theta^2 \\ &= \sum_{j=1}^{N}\sum_{\tau=0}^{T} K_{a,r}(\tau)(E_N[J_{ij}^2x_j^2(t-\tau)] - E_N[J_{ij}x_j(t-\tau)]^2) + \sigma_\theta^2 \\ &= NE_N[J_{ij}^2]\sum_{\tau=0}^{T} K_{a,r}(\tau)E_N[x_j^2(t-\tau)] - NE_N[J_{ij}]^2\sum_{\tau=0}^{T} K_{a,r}(\tau)E_N[x_j(t-\tau)]^2 + \sigma_\theta^2 \\ &= N[\mathrm{var}[J_{ij}] + E_N[J_{ij}]^2]\sum_{\tau=0}^{T} K_{a,r}(\tau)m_N^{(2)}(t-\tau) - N\left(\frac{\bar{J}}{N}\right)^2\sum_{\tau=0}^{T} K_{a,r}(\tau)m_N^{(1)}(t-\tau)^2 + \sigma_\theta^2 \\ &= J^2\sum_{\tau=0}^{T} K_{a,r}(\tau)m_N^{(2)}(t-\tau) + \frac{\bar{J}}{N}\sum_{\tau=0}^{T} K_{a,r}(\tau)m_N^{(2)}(t-\tau) - \frac{\bar{J}}{N}\sum_{\tau=0}^{T} K_{a,r}(\tau)m_N^{(1)}(t-\tau)^2 + \sigma_\theta^2.\end{aligned}$$

Then

$$v_N(t+1) = J^2 \sum_{\tau=0}^{T} K_{a,r}(\tau) m_N^{(2)}(t-\tau) + \frac{\bar{J}}{N} \sum_{\tau=0}^{T} K_{a,r}(\tau)(m_N^{(2)}(t-\tau) - m_N^{(1)}(t-\tau)^2) + \sigma_\theta^2. \tag{B.5}$$

The nth order moments of any function of these normally distributed potentials, $f(h(t))$, integrable with respect to the normal probability measure is

$$m_N^{(n)}(t) = E_N[f^n(h(t))] = \int_{-\infty}^{\infty} f^n(u)(2\pi v_N(t))^{-1/2} \exp\left[\frac{-(u-\mu_N(t))^2}{2v_N(t)}\right] \mathrm{d}u, \tag{B.6a}$$

and after a change of variables

$$m_N^{(n)}(t) = \int_{-\infty}^{\infty} f^n(u\sqrt{v_N(t)} + \mu_N(t))(2\pi)^{-1/2} \exp\left[\frac{-u^2}{2}\right] \mathrm{d}u \tag{B.6b}$$

and for large system size,

$$m^{(n)}(t) = \int_{-\infty}^{\infty} f^n(u\sqrt{v(t)} + \mu(t))(2\pi)^{-1/2} \exp\left[\frac{-u^2}{2}\right] \mathrm{d}u, \tag{B.6c}$$

where $v(t) = \lim_{N\to\infty} v_N(t)$, and $\mu(t) = \lim_{N\to\infty} \mu_N(t)$. Utilizing these results, Eq. (8) can be then derived.

References

[1] R. Kindermann, J.S. Snell, Markov Random Fields and their Applications, Contemporary Mathematics, vol. 1, American Mathematical Society, Providence, RI, 1980.
[2] K.H. Fisher, J.A. Hertz, Spin Glasses, Cambridge University Press, Cambridge, 1991.
[3] D. Stauffer, A. Aharony, Introduction to Percolation Theory, 2nd ed., Taylor & Francis, London, 1994.
[4] W.A. Brock, Pathways to randomness in the economy: emergent nonlinearity and chaos in economics and finance, Estudios Economicos 8 (1) (1993) 3–55.
[5] M.Y. An, N.M. Kiefer, Local externalities and societal adoption of technologies, J. Evol. Econ. 5 (1995) 103–117.
[6] P.A. David, D. Foray, Percolation structures, Markov random fields and the economics of EDI standards diffusion, in: G. Pogorel (Ed.), Global Telecommunications Strategies and Technological Changes, Elsevier, Amsterdam, 1994.
[7] W.A. Brock, S.N. Durlauf, Interactions-based models, in: J. Heckman, E. Leamer (Eds.), Handbook of Econometrics, vol. 5, North-Holland, Amsterdam, 2000.
[8] W.A. Brock, S.N. Durlauf, Discrete choice with social interactions, Rev. Econ. Stud. 28 (2001) 235–260.
[9] M. Aoki, New Approaches to Macroeconomic Modeling: Evolutionary Stochastic Dynamics, Multiple Equilibria, and Externalities as Field Effects, Cambridge University Press, New York, 1996.
[10] D.J. Amit, Modeling brain function: the world of attractor neural networks, Cambridge University Press, New York, 1994.
[11] J. Hertz, A. Krogh, R.G. Palmer, Introduction to the Theory of Neural Computation, Lecture Notes, vol. I, Santa Fe Institute Studies in the Sciences of Complexity, Addison-Wesley, Redwood City, 1991.
[12] S. Amari, Characteristics of random nets of analog neuron-like elements, IEEE Trans. Syst. Man Cybern. 2 (5) (1972) 643–657.
[13] S. Amari, K. Yoshida, K. Kanatani, A mathematical foundation for statistical neurodynamics, SIAM J. Appl. Math. 33 (1) (1977) 95–124.
[14] D. Sherrington, S. Kirkpatrick, Solvable model of a spin glass, Phys. Rev. Lett. 35 (1975) 1792–1796.
[15] S. Kirckpatrick, D. Sherrington, Infinite-ranged models of spin-glasses, Phys. Rev. B 11 (1978) 4384–4403.
[16] H. Sompolinsky, A. Crisanti, H.J. Sommers, Chaos in random neural networks, Phys. Rev. Lett. 61 (3) (1988) 259–262.
[17] A. Crisanti, H. Sompolinski, Dynamics of spin systems with randomly asymmetric bonds: ising spins and Glauber dynamics, Phys. Rev. A 37 (12) (1988) 4865–4874.
[18] B. Doyon, B. Cessac, M. Quoy, M. Samuelides, Control of the transition to chaos in neural networks with random connectivity, Int. J. Bifurc. Chaos 3 (2) (1993) 279–291.
[19] B. Cessac, B. Doyon, M. Quoy, M. Samuelides, Mean-field equations bifurcation map and route to chaos in discrete-time neural networks, Physica D 74 (1994) 24–44.
[20] B. Cessac, Increase in complexity in random neural networks, J. Phys. I 5 (1995) 109–432.
[21] E. Dauce, M. Quoy, B. Cessac, B. Doyon, M. Samuelides, Self-organization and dynamics reduction in recurrent networks: stimulus presentation and learning, Neural Networks 11 (1998) 521–533.

[22] C.F. Manski, Identification of endogenous social effects: the reflection problem, Rev. Econ. Stud. 60 (1993) 531–542.
[23] L.R. Iannacone, Bandwagons and the threat of chaos: interpersonal effects revisited, J. Econ. Behav. Org. 11 (1989) 431–442.
[24] J.B. Rosser, From Catastrophe to Chaos: A General Theory of Economic Discontinuities, Kluwer Academic Publishers, Boston, 1991.
[25] S. Geman, Almost sure stable oscillations in a large system of randomly coupled equations, SIAM J. Appl. Math. 42 (4) (1982) 695–703.
[26] C.J. Emmanouilides, A mean field model with social interactions and network effects in technology diffusion, in: Proceedings of the 26th EMAC Conference, Warwick Business School, May 20–23, 1997, pp. 416–436.
[27] A. Crisanti, G. Paladin, A. Vulpiani, Products of Random Matrices in Statistical Physics, Springer Series in Solid-State Sciences, vol. 104, Springer, New York, 1993.
[28] J.M. Cushing, Integrodifferential Equations and Delay Models in Population Dynamics, Lecture Notes in Biomathematics, vol. 20, Springer, Berlin, 1977.
[29] N.G. Van Kampen, Stochastic Processes in Physics and Chemistry, North-Holland, Amsterdam, 1992.
[30] C.W. Gardiner, Handbook of Stochastic Methods for Physics, Chemistry, and the Natural Sciences, 2nd ed., Springer, Berlin, 1985.
[31] J. Honerkamp, Stochastic Dynamical Systems: Concepts, Numerical Methods, Data Analysis, VCH, New York, 1994.
[32] J.M. Yeomans, Statistical Mechanics of Phase Transitions, Oxford University Press, Oxford, 1992.
[33] A. Lasota, M.C. Mackey, Probabilistic Properties of Deterministic Systems, Cambridge University Press, Cambridge, 1985.
[34] C. Beck, F. Schlogl, Thermodynamics of Chaotic Systems, Cambridge University Press, Cambridge, 1993.
[35] J.P. Eckmann, D. Ruelle, Ergodic theory of chaos and strange attractors, Rev. Mod. Phys. 57 (3) (1985) 617–656.
[36] H.D.I. Abarbanel, Analysis of Observed Chaotic Data, Springer, New York, 1996.
[37] W.A. Brock, W.D. Dechert, J. Scheinkmann, A test for independence based on the correlation dimension, SSRI Working Paper No. 8702, University of Wisconsin, Wisconsin, 1987.
[38] S. Newhouse, D. Ruelle, F. Takens, Occurrence of strange axiom A attractors near quasiperiodic flows on T^m, $m \geq 3$, Commun. Math. Phys. 64 (1978) 35–40.
[39] A. Wolf, J.B. Swift, H.L. Swinney, J.A. Vastano, Determining Lyapunov exponents from a time series, Physica D 16 (1985) 285–317.
[40] R. Gensay, W.D. Dechert, An algorithm for the n Lyapunov exponents of an n-dimensional unknown dynamical system, Physica D 59 (1992) 142–157.
[41] A. Bowman, A. Azzalini, Applied smoothing techniques for data analysis, Oxford University Press, Oxford, 1997.
[42] K. Kaneko (Ed.), Theory and Applications of Coupled Map Lattices, Wiley, New York, 1993.